Graphene bolometer with thermoelectric readout and capacitive coupling to an antenna

Graphene bolometer with thermoelectric readout and capacitive coupling to an antenna

Grigory Skoblin,[1,a)] Jie Sun,[1,2] and August Yurgens[1]
[1]*Department of Microtechnology and Nanoscience, Chalmers University of Technology, 41296 Gothenburg, Sweden*
[2]*Key Laboratory of Optoelectronics Technology, College of Microelectronics, Beijing University of Technology, 100124 Beijing, China*

(Received 18 October 2017; accepted 16 December 2017; published online 5 February 2018)

We report on a prototype graphene radiation detector based on the thermoelectric effect. We used a split top gate to create a *p-n* junction in the graphene, thereby making an effective thermocouple to read out the electronic temperature in the graphene. The electronic temperature is increased due to the AC currents induced in the graphene from the incoming radiation, which is first received by an antenna and then directed to the graphene via the top-gate capacitance. With the exception of the constant DC voltages applied to the gate, the detector does not need any bias and is therefore very simple to use. The measurements showed a clear response to microwaves at 94 GHz with the signal being almost temperature independent in the 4–100 K temperature range. The optical responsivity reached ∼700 V/W. https://doi.org/10.1063/1.5009629

Thermoelectric effects in graphene can be very strong due to its large Seebeck coefficient S (or thermopower, TEP).[1–3] Its value and sign depend on the Fermi level in the graphene, which can be controlled by external gates.[2] This beneficial combination of properties allows for applications such as radiation detectors. Earlier graphene photodetectors were based on the photovoltaic effect.[4–6] However, later studies indicated that photo-thermoelectric effects also play an important role in the detection mechanism,[7–9] especially in a dual-gated device geometry.[10,11] Multiple gates allow for easy creation of *p-n* junctions in graphene, thereby creating a graphene thermocouple to detect the increase in temperature due to the incoming radiation.

In graphene, the electron temperature (T_e) can be significantly higher than the phonon temperature due to a weak coupling between the phonons and electrons.[12–14] Since the Seebeck coefficient depends exactly on the T_e, the thermoelectric voltage can be relatively high even at low base temperatures, where $S(T)$ vanishes. It should be noted that a thermocouple made by connecting graphene and a metal is going to be inefficient, due to active cooling of the electrons in the graphene by the metal. The dual-gated design allows for the creation of an intrinsic graphene thermocouple in or near the hottest region in the graphene, corresponding to the maximum readout voltage. Additionally, the low heat capacitance of monolayer graphene and the even lower heat capacitance of the electrons in the graphene make the response frequency of graphene radiation detectors very high, i.e., in the tens of GHz range.[6,11]

This work introduces a dual-gated graphene bolometer with a thermoelectric readout and capacitive coupling to an antenna. The capacitive coupling in lieu of DC coupling is beneficial because the antenna parts can also be used as the top-gate electrodes, which can significantly simplify the detector design and its operation. Moreover, because of the open-circuit condition for reading out the thermoelectric signal, the requirements for electrical contacts become very relaxed; they can have high resistance without affecting the signal. Our detectors showed a clear response, with the signal being almost temperature independent in the 4–100 K temperature range. The optical responsivity reached ∼700 V/W.

The samples were fabricated with graphene exfoliated on Parylene-N/SiO_2/Si substrates.[15] This technology allows for stable device operation and controlled fabrication of the low-ohmic edge contacts to the graphene. The high-ohmic Si allows the microwave radiation to be coupled to the antenna from below. The combined thickness of the Parylene N and SiO_2 (150 + 90 nm) provides high visibility of the graphene in the optical microscope. After the graphene was exfoliated and monolayer flakes were detected, the sample was immediately covered with another layer of Parylene N to keep the graphene clean and protected from chemicals during the lithography process. The protection reduces parasitic doping and makes the devices stable over time. The device shape and the metal contacts were then defined by e-beam lithography. Oxygen plasma was used to pattern the Parylene/graphene/Parylene sandwich. The Cr/Pd/Au (1/15/200 nm) metal edge-contact electrodes were patterned using the lift-off technique. These electrodes, S1 and S2, had direct ohmic contact with the graphene to measure the TEP signal. An additional layer of Parylene N was deposited to isolate the edges of the graphene from the top-gate electrodes, AG1 and AG2, which were patterned into a log-periodic antenna [see Fig. 1(a)].

To characterize the quality of the graphene, we estimated the field-effect charge-carrier mobility μ at room temperature. At room temperature, the conductivity of the substrate, despite its low doping, was sufficiently high and

a)Author to whom correspondence should be addressed: skoblin@chalmers.se

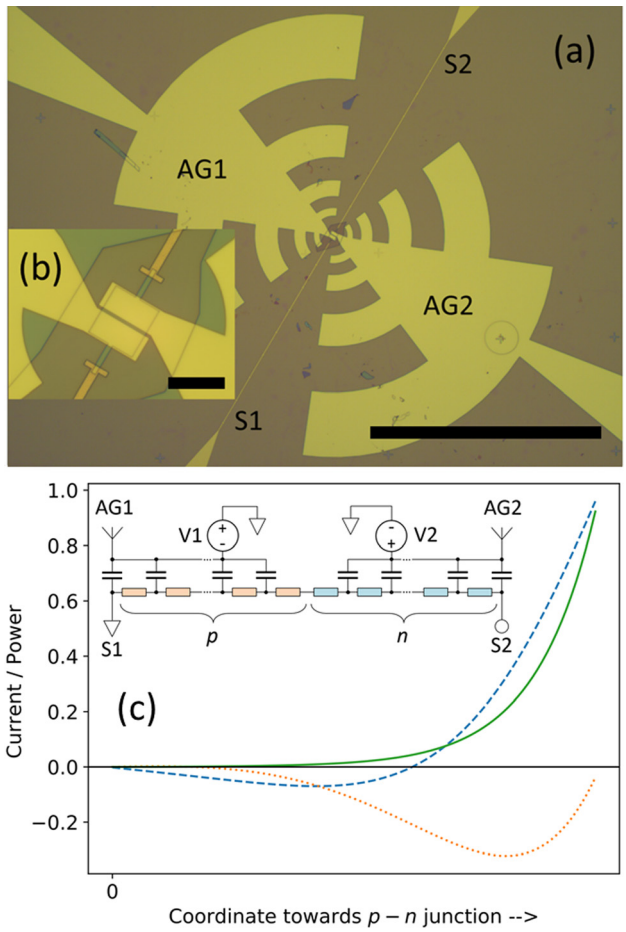

FIG. 1. (a) An overview of a device with a magnified central part (b). The scalebars are 500 μm for (a) and 15 μm for (b). (c) The spatial distribution of the real- and imaginary parts of the AC current in the graphene (dashed blue- and dotted orange curves, respectively). The square of the current (i.e., power) is shown as a solid green curve. The inset in (c) shows the lumped element model of the device. A *p-n* junction is created by applying the DC voltages, *V1* and *V2*, to the top gates, thereby forming an intrinsic thermocouple in the graphene. The antenna parts, AG1 and AG2, are coupled to the graphene through the distributed capacitances, also serving as top gates. The TEP signal is read out as the voltage between S1 and S2.

allowed for using it as a back-gate electrode to tune the charge-carrier concentration in the graphene. The measured transfer characteristic is shown in Fig. 2. Fitting of the two-probe measurements with a model curve gave the low

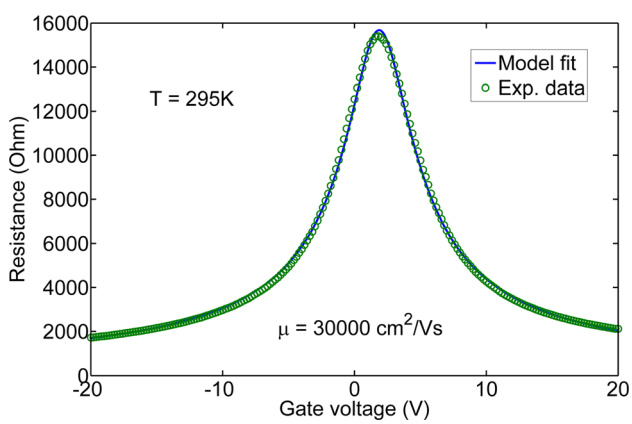

FIG. 2. Two-probe resistance versus back-gate voltage at room temperature. The model fit gives estimations of high mobility ($\sim$30 000 cm^2/V s) and low residual doping (1.0×10^{11} cm^{-2}).

residual doping level ($\sim 1.3 \times 10^{11}$ cm^{-2}) and high charge-carrier mobility ($\sim$30 000 cm^2/V s) of the graphene.

For radiation detection experiments, we mounted the sample in a pulse-tube cryostat with z-cut quartz windows, allowing for optical access to the sample in the 4–300 K range. A Gunn diode with a 94 GHz frequency and 30 mW output power was used as a radiation source outside the cryostat. The power was adjusted by using two attenuators in series (20 dB fixed and 0–50 dB variable). A mechanical chopper at 17–900 Hz modulated the radiation, and the detector signal was synchronously detected using a lock-in amplifier (SR850).

The detector schematic is shown in the inset of Fig. 1(c). The antenna, AG1 and AG2, receives the microwave radiation and directs it to the graphene through the distributed capacitance of the top gate. The radiation and capacitive coupling result in the induced AC current, whose amplitude and phase are functions of the coordinate along the graphene. The Joule heating from the AC current raises the electronic temperature in the graphene. The same electrodes (AG1 and AG2) are used to create the intrinsic *p-n* junction in the graphene by applying different voltages, V_1 and V_2, to them. The increased electronic temperature can then be detected by measuring the thermoelectric voltage between the S1 and S2 contacts. As we noted earlier, these electrodes are efficient thermal reservoirs for electrons and cool the nearby graphene parts. Overall, this creates a temperature gradient from the *p-n* junction in the center of the graphene down to the electrodes and gives rise to the TEP signal.

It should be emphasized that the capacitive coupling of the antenna to the graphene is especially beneficial because it ensures that the maximum Joule dissipation occurs close to the *p-n* junction, thereby yielding the maximum efficiency for the signal detection. Indeed, the lumped element model for our device allows for the calculation of the spatial distribution of the AC current and corresponding Joule power [see Fig. 1(c)]. The calculation showed that the Joule dissipation occurs mostly close to the *p-n* junction, increasing the electronic temperature at that point [see the green solid line in Fig. 1(c)]. In the other case of direct electrical contacts for the antenna electrodes to the graphene, the Joule heating would take place everywhere, which would also include the parts that are far away from the *p-n* junction. Thus, the radiation power would be spread out over some auxiliary graphene parts that do not contribute to a useful signal. Clearly, this would limit the responsivity of the device.

We measured the TEP signal V_{TEP} as a function of the top-gate voltage (± 10 V) and the temperature $T = 4$–295 K at a constant radiation power of the source. Fixing the difference between the top-gate voltages, $\delta V = V_1 - V_2$, we swept the mean value $V_g = (V_1 + V_2)/2$ and measured V_{TEP}. In Fig. 3(a), we present a series of such measurements for different δV at 50 K. We see that $|V_{\mathrm{TEP}}|$ reaches the maximum at $\delta V = \pm 4$ V and $V_g \approx 3$ V. The latter roughly corresponds to the position of the charge-neutrality point in the sample (see Fig. 2). In Fig. 3(b), we present simulations of the TEP curves. For this analysis, we use a simple equation

$$V_{\mathrm{TEP}} = (S(V_1) - S(V_2))\Delta T,$$

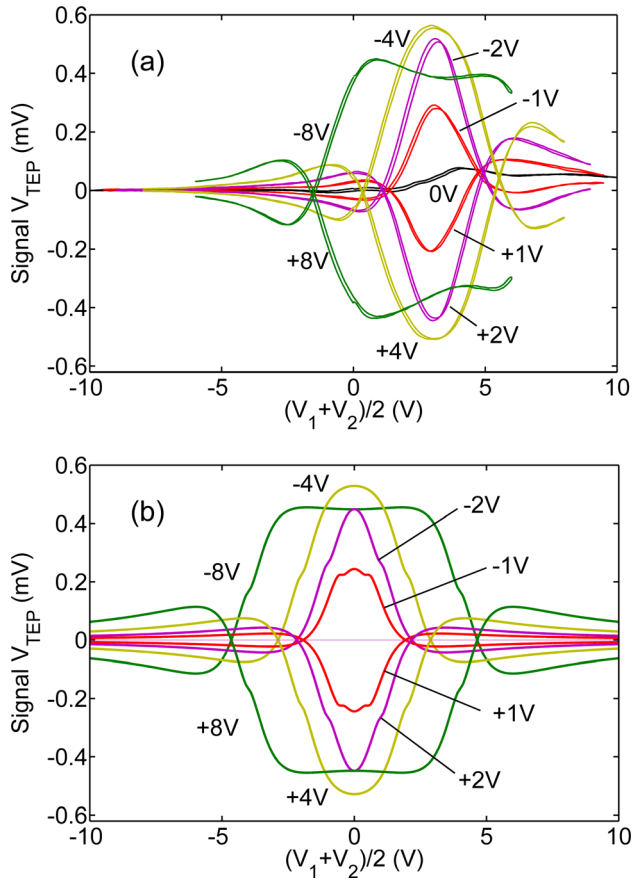

FIG. 3. (a) The TEP signal as a function of the mean top-gate voltage for various voltage differences $\delta V = V_1 - V_2$ at $T = 50$ K. The maximum signal occurs at $\delta V = \pm 4$ V. At zero δV, almost no signal occurs due to the equal Seebeck coefficients induced. (b) Simulation of the TEP signal as a function of the mean top-gate voltage for the same set of δV, $T = 50$ K, and $n_0 = 10^{11}$ cm^{-2}.

where ΔT is the average overheating of the electron system, and $S(V_1)$ and $S(V_2)$ are the Seebeck coefficients of the two top-gated parts of the graphene described by Mott's formula[16]

$$S(V) = -\frac{2\pi^{\frac{3}{2}}}{3}\frac{k_B^2 T}{\hbar v_F \sqrt{e}}\frac{(C_g V)^{\frac{3}{2}}}{(en_0)^2 + (C_g V)^2},$$

where V is the voltage applied to the top gate, $C_g = 1.5 \times 10^{-4}$ F/m^2 is the gate capacitance per unit area, $n_0 = 10^{11}$ cm^{-2} is the residual carrier concentration, $\hbar$ is the Planck constant, v_F is the Fermi velocity, k_B is the Boltzmann constant, and e is the proton charge. We see a good qualitative agreement between the experimental results and the simulations. By adjusting ΔT, we find that the maximum signal in the simulations is close to the experimental value at $\Delta T = 7$ K for $\delta V = \pm 4$ V and $T = 50$ K.

In Figs. 4(a) and 4(b), we present the temperature dependencies of the detector signal, taken at the optimal gate-voltage difference. The $\sim$600 μV signal does not depend on temperature in the range of 4–100 K. However, at room temperature, the signal is weak ($\sim$10 μV). As mentioned above, the device was fabricated on a low-doped Si substrate, which was slightly conducting at room temperature and would therefore partially screen out the radiation from the source. This explains the low signal observed at room temperature. At temperatures below 100 K, the charge-carriers freeze out and let the radiation penetrate the substrate without any significant attenuation.

It is noteworthy that the TEP signal is independent of temperature below 100 K. Indeed, the Seebeck coefficient of graphene is proportional to temperature, $S(T) \sim T/3$ [μV/K],[3] so one would expect a significant decrease in the TEP signal at low temperatures, which is clearly not the case in the experiments [see Figs. 4(a) and 4(b)]. This suggests that the decrease in $S(T)$ is counterbalanced by the increase in electronic temperature—the lower the bath temperature, the higher the increase. Indeed, the electronic temperature results from equilibrium between the radiation power and the cooling power P. The cooling of electrons occurs mainly via their interactions with phonons, $P \propto \left(T_e^m - T_{ph}^m\right)$, where T_{ph} is the phonon temperature and $m \approx 3$–4 depending on the details of the interaction.[17,18] The phonon temperature is usually very close to the bath (ambient) temperature T_0.

To characterize our detector, we measured its responsivity and the noise-equivalent power (NEP) at 50 K. In Fig. 4(c), we present a plot of the detector signal vs. power attenuation at 50 K. Without attenuation, the signal is $V_s \approx 700$ μV. From the geometry of our setup, we estimate the power reaching our device to be $\sim$1 μW; the corresponding responsivity is then $\sim$700 V/W. The linear response saturates at $\sim$40 dB of attenuation. This corresponds to $\sim$100 pW of the power transferred to the sample. Taking into account the equivalent noise bandwidth of 0.26 Hz, we get a NEP of $\sim$200 pW/Hz$^{0.5}$. This estimation is still very conservative, because the measurements were performed with high electric

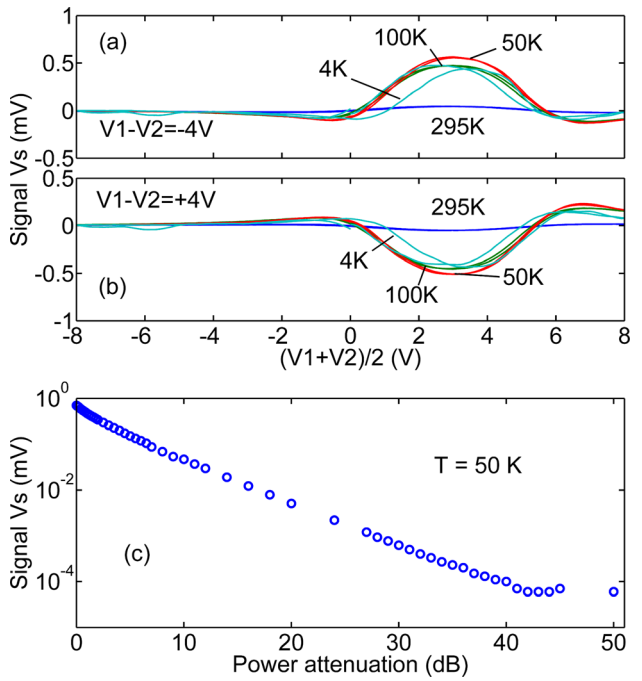

FIG. 4. The TEP signal as a function of the mean top-gate voltage for different temperatures at the fixed voltage difference of +4 V (a) and −4 V (b). For the 4100 K range, the signal is almost temperature independent. At T = 4 K, we see a hysteresis which is caused by the remaining charge-carriers in the substrate. Plot (c) is the dependence of the signal on the power attenuation at the gate-voltage difference of −4 V and the mean gate voltage of 3 V, corresponding to the maximum signal at $T_0 = 50$ K. The signal disappears in a rather high background noise above 40 dB of attenuation.

background noise caused by the powerful compressor of the pulse-tube cryostat. With the compressor switched off, the background voltage noise of our measurement system usually drops down to some 10–20 $nV/Hz^{0.5}$. This corresponds to an approximately ten times smaller NEP of ~15–30 $pW/Hz^{0.5}$. There is also room for improvement in terms of the responsivity, which comes from the antenna impedance mismatch. The theoretical impedance of the log-periodic antenna we used is 190 Ω, whereas the resistance of the graphene device is ~10 kΩ. This leads to 50 times less power reaching the device than in the case of matched impedance. Thus, after optimization of the antenna-graphene coupling, the responsivity can be improved by about two orders of magnitude.

To summarize, we introduced a graphene radiation detector with a thermoelectric readout of an enhanced electronic temperature due to the radiation. The key feature of the detector is the capacitive coupling between the antenna and the graphene allowing for a simple design with a relaxed requirement for the contact resistance to the graphene. The graphene is completely encapsulated in a polymer making the detector stable over time. Our detector has a responsivity of ~700 V/W and a noise-equivalent power of <200 $pW/Hz^{0.5}$ at 50 K.

We are grateful for the financial support from the Swedish Research Council, the Swedish Foundation for Strategic Research, and the Knut and Alice Wallenberg Foundation. J. Sun acknowledges the National Natural Science Foundation of China (11674016), National Key R&D Program (2017YFB0403102), Beijing Municipal Commission of Science and Technology (Z161100002116032), and Swedish Foundation for International Cooperation in Research and Higher Education (CH2015-6202).

[1]D. Philippe, N. Viet Hung, and S.-M. Jérôme, J. Phys. Condens. Matter **27**, 133204 (2015).
[2]P. Wei, W. Bao, Y. Pu, C. N. Lau, and J. Shi, Phys. Rev. Lett. **102**, 166808 (2009).
[3]Y. M. Zuev, W. Chang, and P. Kim, Phys. Rev. Lett. **102**, 096807 (2009).
[4]E. J. H. Lee, K. Balasubramanian, R. T. Weitz, M. Burghard, and K. Kern, Nat. Nanotechnol. **3**, 486 (2008).
[5]J. Park, Y. H. Ahn, and C. Ruiz-Vargas, Nano Lett. **9**, 1742 (2009).
[6]F. Xia, T. Mueller, Y.-M. Lin, A. Valdes-Garcia, and P. Avouris, Nat. Nanotechnol. **4**, 839 (2009).
[7]Q. Han, T. Gao, R. Zhang, Y. Chen, J. Chen, G. Liu, Y. Zhang, Z. Liu, X. Wu, and D. Yu, Sci. Rep. **3**, 3533 (2013).
[8]A. L. Hsu, P. K. Herring, N. M. Gabor, S. Ha, Y. C. Shin, Y. Song, M. Chin, M. Dubey, A. P. Chandrakasan, J. Kong, P. Jarillo-Herrero, and T. Palacios, Nano Lett. **15**, 7211 (2015).
[9]X. Xu, N. M. Gabor, J. S. Alden, A. M. van der Zande, and P. L. McEuen, Nano Lett. **10**, 562 (2010).
[10]N. M. Gabor, J. C. W. Song, Q. Ma, N. L. Nair, T. Taychatanapat, K. Watanabe, T. Taniguchi, L. S. Levitov, and P. Jarillo-Herrero, Science **334**, 648 (2011).
[11]J. Yan, M. H. Kim, J. A. Elle, A. B. Sushkov, G. S. Jenkins, H. M. Milchberg, M. S. Fuhrer, and H. D. Drew, Nat. Nanotechnol. **7**, 472 (2012).
[12]A. C. Betz, S. H. Jhang, E. Pallecchi, R. Ferreira, G. Feve, J. M. Berroir, and B. Placais, Nat. Phys. **9**, 109 (2013).
[13]R. Bistritzer and A. H. MacDonald, Phys. Rev. Lett. **102**, 206410 (2009).
[14]J. Jens Christian, U. Søren, B. Marco, H. Richard, G. Dandan, M. Federico, H. Liv, F. Felix, R. Christian, S. Thomas, and H. Philip, J. Phys. Condens. Matter **25**, 094001 (2013).
[15]G. Skoblin, J. Sun, and A. Yurgens, Appl. Phys. Lett. **110**, 053504 (2017).
[16]J. C. Song, M. S. Rudner, C. M. Marcus, and L. S. Levitov, Nano Lett. **11**, 4688 (2011).
[17]S. S. Kubakaddi, Phys. Rev. B **79**, 075417 (2009).
[18]J. K. Viljas and T. T. Heikkilä, Phys. Rev. B **81**, 245404 (2010).